Visible and terahertz nonlinear responses in the topological noble metal dichalcogenide $PdTe_2$

George J. de Coster,[1,2,*,†] Lucas Lafeta,[3,*,‡] Stefan Heiserer,[1] Cormac Ó Coileáin,[1] Zdenek Sofer,[4] Achim Hartschuh,[3] Georg S. Duesberg,[1] and Paul Seifert[1,§]

[1]*Institute of Physics and Center for Integrated Sensor Systems (SENS), University of the Bundeswehr Munich, Werner-Heisenberg-Weg 39, 85577 Neubiberg, Germany*

[2]*DEVCOM Army Research Laboratory, 2800 Powder Mill Road, Adelphi, Maryland 20738, USA*

[3]*Department of Chemistry and Center for NanoScience (CeNS), Ludwig-Maximilians-Universität München, Butenandtstraße 5-13 (E), 81377 Munich, Germany*

[4]*Department of Inorganic Chemistry, University of Chemistry and Technology Prague, Technická 5, 166 28 Prague 6, Czech Republic*

(Received 26 November 2025; accepted 13 March 2026; published 20 April 2026)

Nonlinear processes can offer pathways to next-generation sensors and frequency mixing devices to overcome modern imaging, detection, and communication challenges. In this article, we report on strong second- and third-order nonlinear optical responses in visible and terahertz light in single crystals of the noble metal dichalcogenide $PdTe_2$. We find that buried conduction and valence topological surface states of $PdTe_2$ lead to resonant optical second-harmonic generation. On the other hand, although the nonlinear responses obtained with terahertz excitation are not close to this resonance, they can be clearly observed in reflection geometry, even in the presence of broadband excitation, where optical filters are not necessary to observe the enhanced odd-order higher harmonic output. By carefully considering the radiative photocurrent framework of stimulated terahertz emission, we are able to extract fingerprints of both second- and third-order processes in the terahertz regime, and show that $PdTe_2$ is a promising material candidate for radio-frequency rectification, frequency mixing, and beam focusing.

DOI: 10.1103/x5kl-blc5

I. INTRODUCTION

Quantum materials with strong spin-orbit coupling and topological surface states have spawned new device concepts that exploit nonlinear optical (NLO) rectification and higher-harmonic generation [1–4], the Josephson diode effect [5,6], and spin-orbit torque switching [7,8]. NLO responses in quantum materials are particularly relevant to polarization-sensitive imaging, frequency conversion, and radio-frequency (rf) detection, as even inversion-symmetric crystal systems can exhibit strong second-harmonic generation (SHG), polarization-dependent photocurrent generation, and rectification processes classically forbidden by symmetry [1,9–12]. Such effects often originate from topological surface states, which enable broadband photocurrent and DC rectification spanning near-UV to terahertz frequencies [10,13–15].

Layered noble metal dichalcogenides (NMDs), (Pd, Pt)(Te,Se,S)$_2$, have recently been recognized as a distinctive class of two-dimensional (2D) quantum materials, which combine metallic conductivity, strong spin-orbit coupling, and topologically nontrivial electronic structures. They crystallize predominantly in the centrosymmetric 1T phase (space group $P\bar{3}m1$) with octahedral coordination of the transition metal [Figs. 1(a) and 1(b)], and have recently been shown to be accessible via low-temperature synthesis methods [16,17]. Among them, $PdTe_2$ is a type-II Dirac semimetal which hosts both topological surface states and superconductivity [18,19]. Related compounds such as $PtTe_2$ and $PtSe_2$ exhibit nonsaturating magnetoresistance, high carrier mobilities, and thickness-driven band-structure evolution from semimetallic to semiconducting behavior [18,20–25]. Despite their inversion symmetry, NMDs display unexpectedly strong NLO effects, including SHG, shift currents, and photogalvanic responses, attributed to local symmetry breaking, surface and interface fields, or strain-induced distortions [26–30]. Their large second-order susceptibilities are enhanced by spin-orbit coupling and Berry curvature effects, making them promising candidates for tunable NLO devices. Their 2D nature allows straightforward integration into micro-electromechanical systems (MEMS) architectures and tuning via thickness control, Janus engineering, or strain [2,31–35].

In this work, we verified the crystalline quality and symmetry of the $PdTe_2$ flakes using Raman spectroscopy [Fig. 1(c) and 1(d)], showing the characteristic E_g and A_{1g} phonon modes, and by lattice-resolution atomic force microscopy (AFM) imaging [Fig. 1(e)], revealing the expected hexagonal surface lattice (0.39 nm lattice constant). A representative bulk crystal is shown in Fig. 1(c), and the schematic band

*These authors contributed equally to this work.
†Contact author: george.j.decoster.civ@army.mil
‡Contact author: lucas.lafeta@cup.lmu.de
§Contact author: paul.seifert@unibw.de

Published by the American Physical Society under the terms of the Creative Commons Attribution 4.0 International license. Further distribution of this work must maintain attribution to the author(s) and the published article's title, journal citation, and DOI.

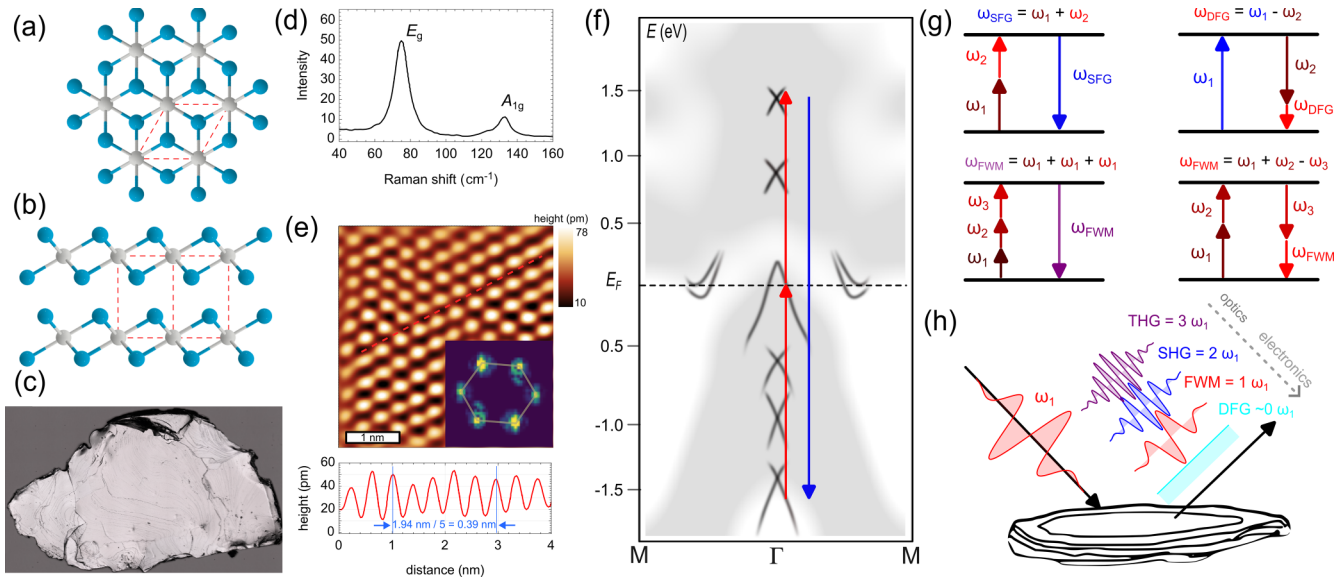


FIG. 1. (a) Top view and (b) side view of 1T layered crystal structure of $PdTe_2$ with Pd atoms shown in gray and Se atoms shown in blue. (c) Optical microscopy image of an approximately 5-mm bulk layered $PdTe_2$ crystal. (d) Raman spectrum of $PdTe_2$. (e) Lattice-resolution AFM image (Fourier filtered), with profile along the dashed red line (below). Inset: Fast Fourier transform of the AFM image. (f) Schematic electronic structure of $PdTe_2$ along the Γ-M direction with bulk bands indicated in gray and surface (projected) bands and topological surface states indicated in black. A possible resonant condition for SHG is shown by the arrows (red, excitation; blue, emission). (g) Generic second- and third-order sum-frequency generation (SFG), second-order difference-frequency generation (DFG), and third-order four-wave mixing (FWM) processes, highlighting the energy exchange between interacting photons. (h) Schematic illustration of SHG, THG, FWM, and DFG processes from a near-monochromatic wave packet.

structure [Fig. 1(f)] illustrates the type-II Dirac dispersion with topological surface states and surface-projected Dirac cones.

Moreover, we demonstrate NLO and harmonic generation in $PdTe_2$ in both the visible (about 1.5 eV) and terahertz range (about 0.1–3 THz), revealing persistent and tunable nonlinear responses in this centrosymmetric topological semimetal. These responses at disparate optical bands invite a closer examination of the nonlinear mechanisms that can arise in layered systems such as $PdTe_2$. We outline the fundamental principles of NLO interactions in 2D materials, emphasizing how local symmetry breaking and spin-orbit-driven band topology can enhance their nonlinear susceptibilities.

II. PRINCIPLES OF NONLINEAR OPTICS IN TWO-DIMENSIONAL MATERIALS

NLO techniques have become essential tools for probing 2D materials. SHG, a second-order process, is widely used to determine lattice orientation and symmetry in noncentrosymmetric systems such as hexagonal boron nitride (h-BN) and transition metal dichalcogenides (TMDs) [36–38], while third-order techniques like four-wave mixing (FWM) probe resonant transitions and excitonic responses [39]. The optical response of a medium arises from the induced polarization $\mathbf{P}(\mathbf{r}, t)$ caused by the incident electric field $\mathbf{E}(\mathbf{r}, t)$:

$$\mathbf{P} = \varepsilon_0(\chi^{(1)}\mathbf{E} + \chi^{(2)}\mathbf{E}^2 + \chi^{(3)}\mathbf{E}^3 + \cdots), \tag{1}$$

where $\chi^{(n)}$ is the nth-order susceptibility tensor. At low field intensities, the linear term ($\chi^{(1)}$) dominates, whereas higher intensities activate nonlinear terms. The tensor rank grows with order ($\chi^{(1)}$, 9 elements; $\chi^{(2)}$, 27; $\chi^{(3)}$, 81), and the nonvanishing elements are dictated by crystal symmetry [40]. Even-order processes vanish in perfectly centrosymmetric materials ($\chi^{(2n)} = 0$), implying that SHG and related effects arise only when inversion symmetry is locally broken. In frequency space the second-order nonlinear polarization responsible for SHG is given by

$$\mathbf{P}^{(2)}(2\omega_1) = \varepsilon_0\chi^{(2)}\mathbf{E}(\omega_1)\mathbf{E}(\omega_1), \tag{2}$$

which corresponds to the second-order sum-frequency process in Fig. 1(g) with $\omega_1 = \omega_2$. The third-order term corresponding to FWM is

$$\mathbf{P}^{(3)}(2\omega_1 - \omega_3) = \varepsilon_0\chi^{(3)}\mathbf{E}(\omega_1)\mathbf{E}(\omega_1)\mathbf{E}^*(\omega_3). \tag{3}$$

This particular degenerate case of third order corresponds to the bottom third-order optical process in Fig. 1(g) with $\omega_1 = \omega_2$. It gives rise to sum- and difference-degenerated FWM [40]. The spectral dependence of the nonlinear response tensors is discussed in Secs. III and IV. We note here that enhancements to SHG and FWM are anticipated when the excitation pathways or emission correspond to resonances within the band structure [39], as indicated by the resonant SHG process at 2.95 eV in Fig. 1(f).

The form and symmetries of $\chi^{(2)}$ and $\chi^{(3)}$ are easily computed using the C_{3v} surface point group of 1T-$PdTe_2$. These results are well known and not shown here [41–43]. When bulk inversion symmetry is further imposed on the tensors, $\chi^{(2)}$ becomes trivially zero. In centrosymmetric materials like $PdTe_2$, strong spin-orbit coupling, surface states, and strain fields can locally break inversion symmetry and amplify Berry curvature effects, resulting in finite $\chi^{(2)}$ and enhanced

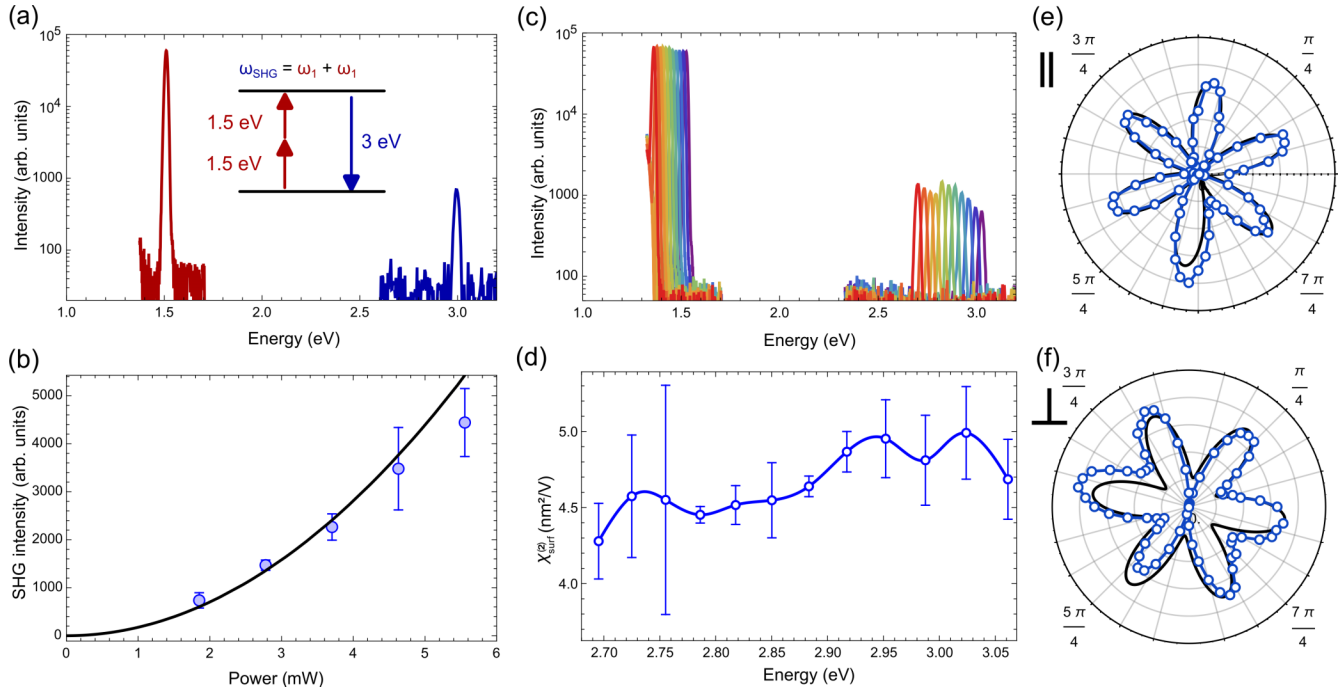


FIG. 2. (a) Optical second-harmonic generation at 3 eV in $PdTe_2$ stimulated by a 1.5-eV pulsed laser. (b) The power dependence of the SHG at 3 eV is shown to be quadratic in the pulse power, consistent with SHG scaling. (c) Spectra of excitation and SHG emission for varying excitation wavelength. (d) Experimental values of $PdTe_2$ surface $\chi^{(2)}$, extracted by comparative method using crystalline quartz as a reference sample, for different wavelengths. The symmetry of the (e) parallel and (f) cross polarization of the SHG response to varying the polarization of the 1.5-eV pulse by a half-wave plate synchronous with a polarizer in front of the detector is checked and found to exhibit sixfold symmetry consistent with the C_{3v} surface point group of $PdTe_2$.

$\chi^{(3)}$. These mechanisms provide a natural explanation for the broadband nonlinear and harmonic generation responses observed experimentally.

III. NONLINEAR OPTICAL RESPONSES TO VISIBLE LIGHT IN $PdTe_2$

A. Second-harmonic generation

The emission of SHG in noble metal dichalcogenides has been investigated previously [26,29,44]. Despite the inversion symmetry of the point group D_{3d} ($P\bar{3}m1$ space group) for the 1T phase [see Figs. 1(a) and 1(b)], experiments have seen nonzero emission of SHG by the surface of $PdTe_2$, governed by the C_{3v} point-group symmetries of the surface [26]. In our studies, we focus the experiments on the $PdTe_2$ sample shown in Fig. 1(c). To probe second-harmonic generation, we excite $PdTe_2$ with a pulsed 1.5-eV (about 825 nm) laser, generating a second-order signal at 3 eV (about 412.5 nm). Figure 2(a) shows the observed spectra of the emission of the SHG in blue and the residual incident field after the short pass in red.

The quadratic power dependence of the SHG intensity is shown in Fig. 2(b) using the same condition as measured in Fig. 2(a). This quadratic behavior is characteristic of the second-order process, thereby corroborating the second-harmonic generation in $PdTe_2$. Figure 2(c) presents the spectra of SHG using various wavelengths; the region at 1.5 eV shows the incident field after short-pass filtering. The peaks near 3 eV are SHG at the corresponding incident wavelengths.

The second-order nonlinear susceptibility of the $PdTe_2$ surface ($\chi^{(2)}$) was measured using a comparative method with crystalline quartz as a reference sample [36,39] and the values of $\chi^{(2)}$ for different wavelengths are shown in Fig. 2(d). The method used to obtain the $\chi^{(2)}$ value, and a comparison with other materials (such as monolayers of WS_2, MoS_2, and $MoSe_2$), are discussed in Appendix B.

Figures 2(e) and 2(f) respectively show the experimental polar dependency of the SHG signal upon rotating the incident electric field synchronously with the polarizer in the detection parallel and perpendicular, respectively. The sixfold rotational symmetry of the polarization intensity is the signature of an underlying threefold rotation-symmetric lattice. The data are closely fit by the functional form (black) expected for surface C_{3v} point-group symmetry [41,42]. The defects, on the other hand, possess a generic twofold rotational symmetry of their SHG spectrum (see Appendix A), which follows from many point groups and thus only serves to show the defects break the symmetry of the parent lattice.

B. Four-wave mixing

We next investigated the third-order nonlinear regime using FWM, which, unlike second-order processes, does not rely on symmetry breaking and is allowed in all media. FWM provides direct access to the third-order susceptibility $\chi^{(3)}$, offering insight into the intrinsic electronic nonlinearity of $PdTe_2$. Special cases such as third-harmonic generation (THG) and degenerate FWM (DFWM) have been widely used to probe materials, including h-BN, graphene, carbon nanotubes, and TMDs [45–50].

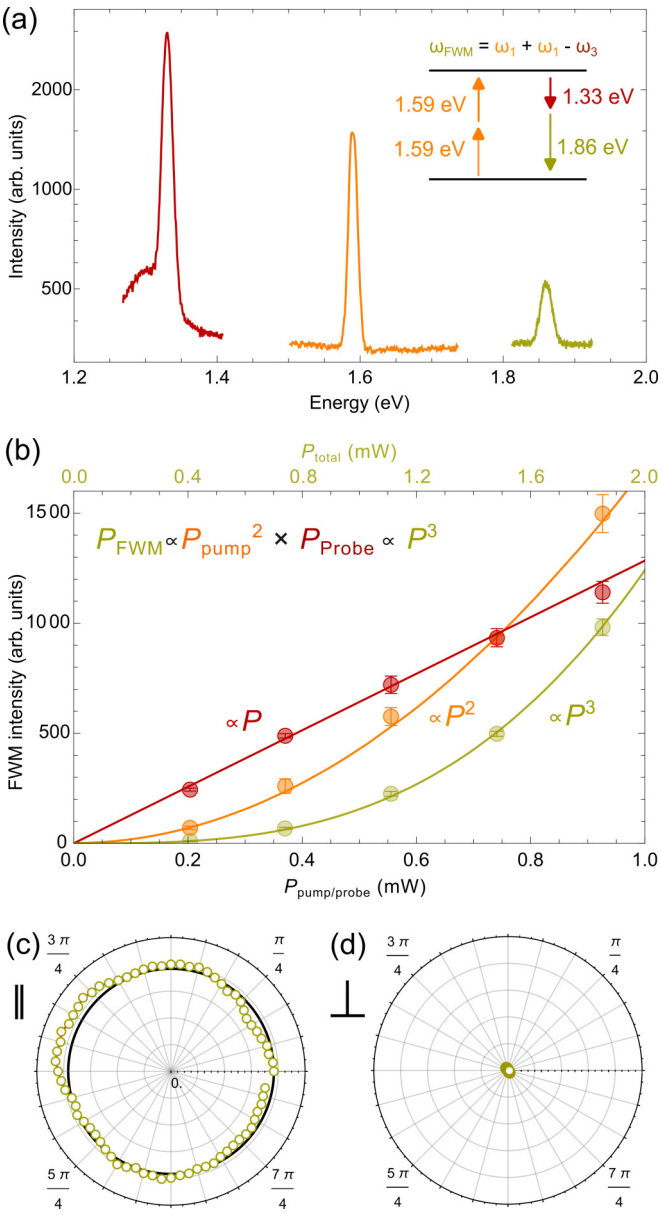


FIG. 3. (a) Optical FWM probing of the third-order nonlinear response of $PdTe_2$ is conducted using 1.59-eV and 1.33-eV pump and probe pulses. (b) The power dependence of the FWM intensity is quadratic in pump intensity and linear in probe intensity, yielding an overall cubic intensity dependence, consistent with a third-order effect. The input fields were subjected to a half-wave-plate rotation of their polarization, and the symmetry of the (c) parallel and (d) cross polarization-detected fields was probed. Consistent with C_{3v} surface point-group symmetry, there is effectively no third-order response at cross polarization, and a constant signal for the parallel detection.

We demonstrate a DFWM process in bulk $PdTe_2$ samples. Figure 3(a) shows the FWM spectrum generated by two degenerate pump fields at 1.59 eV (about 780 nm) and one probe at 1.33 eV (about 932 nm), producing a fourth wave at 1.86 eV (about 667 nm). Figure 3(b) presents the power dependence of the FWM signal, which follows the proportion $I_{FWM} \propto I_{pump}^2 I_{probe}$. When the pump power is fixed at about 1.1 mW and the probe power is varied, the FWM intensity shows linear scaling with I_{probe} (red curve). Inversely, by fixing the probe power at about 1.1 mW and varying the pump power, the FWM intensity then scales as I_{probe}^2 (orange curve). The FWM intensity scaling can be calculated from the combination of these two measurements, and results in a cubic scaling with total input power (green curve).

We further probed the symmetries of the FWM signal by subjecting both pump and probe incident laser to half-wave-plate rotations by synchronously rotating a polarizer in front of the detector, and then collecting the resulting signal at parallel and cross polarizations to the incident beams. The results in Figs. 3(c) and 3(d) show near-uniform behavior as a function of wave-plate angle, with almost no signal present in the cross-polarization detection. This is consistent with the symmetry of $PdTe_2$ for third-order processes. The slight deviations from uniformity in Fig. 3(c) can be attributed to the optical setup efficiency in certain polarization directions and alignment of the wave-plate angle with the polarizer in the detection.

The observation of a strong DFWM signal in $PdTe_2$ reveals a clear third-order nonlinear susceptibility ($\chi^{(3)}$). The effective third-order nonlinear susceptibility can be extracted using a comparative method [39] (analogous to the second-order case shown earlier) with a well-established reference (in this case, fused quartz). The effective $\chi^{(3)}$ for a bulk sample of $PdTe_2$ found using the same wavelength as shown in Fig. 3(a) was $\chi^{(3)}_{eff} \approx 2 \times 10^{-21}$ m^2/V^2 (further information and discussion can be found in Appendix B). This response can arise from contributions of Dirac-like interband transitions and surface electronic states, which potentially enhance $\chi^{(3)}$ even in metallic systems [51–56]. This highlights $PdTe_2$ as a promising platform for broadband nonlinear photonics that extends beyond the family of semiconducting 2D materials.

IV. TERAHERTZ SPECTROSCOPY

By investigating the response of $PdTe_2$ to terahertz radiation, we can determine if the NLO activity of interband transitions probed by SHG and FWM disappears for smaller, intraband energy scales (1 THz corresponds to 4.14 meV). Similarly to our experiments at optical frequencies, we performed terahertz time-domain spectroscopy on the $PdTe_2$ in atmosphere under reflection geometry using a pulse centered around 0.7 THz. The reflected pulse was sampled in time, and a pulse reflected off a gold mirror was used as a reference signal to determine the spectrum of the excitation pulse.

The time-domain signal of a reference pulse and the terahertz pulse generated by reflecting off the $PdTe_2$ crystal surface are shown in Fig. 4(a). In Fig. 4(b) we show the spectrum of these two pulses where clear dips corresponding to absorption by atmospheric water vapor can be seen. We find that the time-integrated power of the pulse emitted by $PdTe_2$ is lower than the reference pulse. However, for particular frequency bands, $f < 0.2$ THz and $1.5 < f < 2.7$ THz, the spectral intensity emitted by $PdTe_2$ is higher than the spectral intensity of the reference pulse. This is a clear indication of nonlinear optical activity that enhances the output at these frequencies. In particular, the low-frequency, near-DC behavior can only arise from frequency-difference processes in an even-order nonlinear response, such as optical rectification

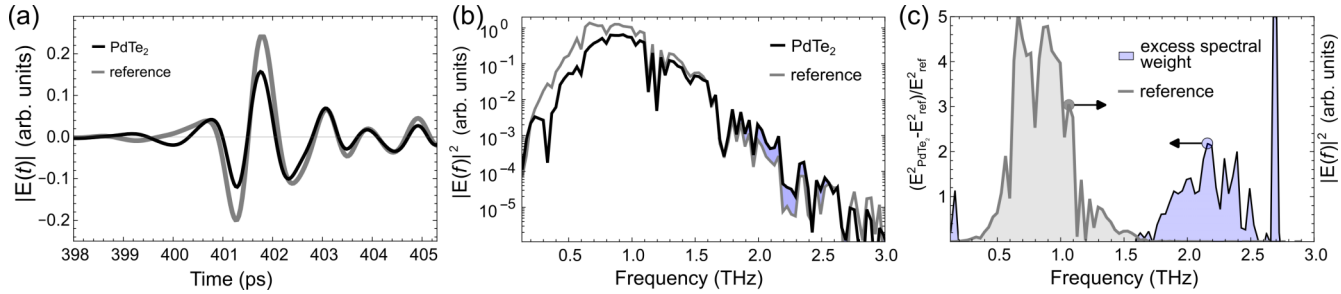


FIG. 4. (a) Time scans of the reference injected terahertz pulse and that emitted by $PdTe_2$ after illumination. The pulses are overlaid to show their qualitative difference. (b) Their intensity Fourier spectra show the $PdTe_2$ emission is greater than the reference for some higher and lower frequencies. (c) Excitation spectrum (gray) and relatively enhanced spectral weight in the reflected pulse (blue).

or photogalvanic or photon drag effects, since the excitation pulse does not have spectral contributions at such low frequencies [10,43]. Given the broad bandwidth of our excitation pulse, however, multiple higher-harmonic generation (HHG) orders could conceivably contribute to the observed enhanced spectral output, since the individual contributions cannot be clearly separated as in the visible NLO experiments.

To determine which HHG orders are present within the $PdTe_2$ spectrum, we performed a power-dependence study. Using a pair of polarizers placed after the terahertz emitter, we varied the orientation of the first while keeping the second fixed. As a result, we can fit the spectrum $E_{\mathrm{rad}}(f)$ as a function of the power P for each frequency f. The injected and emitted electric fields, $E_{\mathrm{in}}(f)$ and $E_{\mathrm{rad}}(f)$, are complex. By assuming $|E_{\mathrm{in}}(f)| = \mathcal{E}_0\sqrt{P}$ for some frequency-independent constant $\mathcal{E}_0$ we can derive a fitting equation for the real-valued spectrum as a function of power, $|E_{\mathrm{rad}}(f,P)|^2$:

$$|E_{\mathrm{rad}}(f,P)|^2 = |\chi^{(1)}(f)P^{1/2} + \chi^{(2)}(f)P + \chi^{(3)}(f)P^{3/2}|^2. \quad (4)$$

We have now absorbed powers of $\mathcal{E}_0$ into $\chi^{(n)}$. The power dependence and corresponding fits at the pulse center frequency, as well as its multiples and in the low-frequency limit, are shown in Fig. 5(a). The linear response, SHG, and THG coefficients $|\chi^{(n=1,2,3)}(f)|$ are shown in Fig. 5(b). We note that although quadratic and cubic terms are mathematically independent, over the limited available power range with dominant linear response they become nearly collinear. Consequently, the fit converges to the dominant higher-order term rather than distributing weight across both.

From this analysis, we can conclude that the enhanced spectral output at high frequencies in Fig. 4(c) is due to THG, and the low-frequency excess is indeed due to a second-order process. Moreover, there is a strong third-order fundamental enhancement at the terahertz spectral peak, indicating that for high enough powers or narrow enough terahertz pulses, $PdTe_2$ could be used for pulse refocusing. We note that while we can distinguish the SHG of the bare $PdTe_2$ surface from the one generated by symmetry-breaking defects and edges, etc., in visible experiments, the large spot size diameter of 300–500 μm in terahertz experiments makes these contributions indistinguishable. However, we believe the overall SHG intensity to be dominated by the bigger area of bare $PdTe_2$ surface.

We can compare the power analysis to the theoretically predicted HHG spectrum for the incoming pulse. The energy scales of terahertz spectroscopy (1 THz ≈ 4 meV) are far below the interband transitions we studied with visible excitations, and the technique is often employed to probe

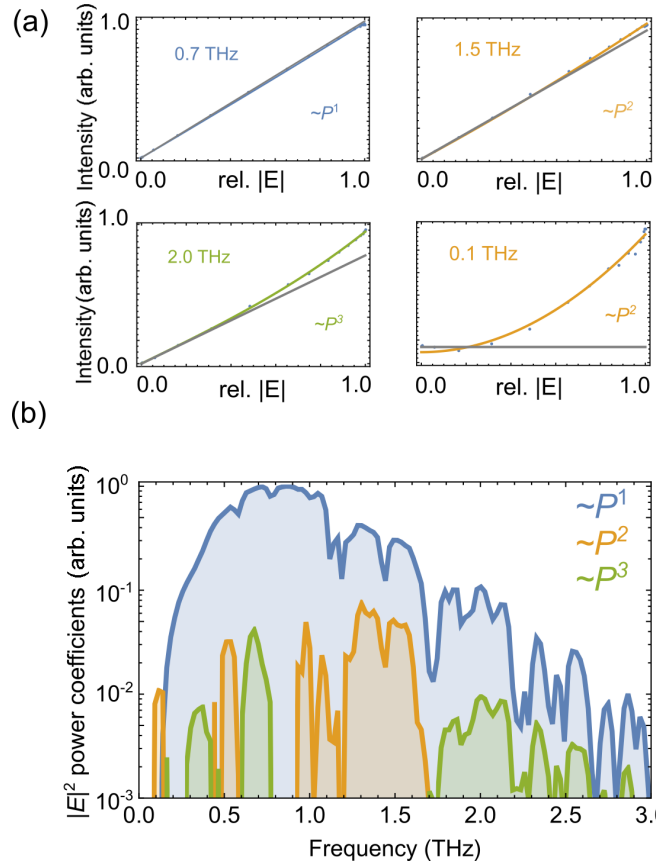


FIG. 5. (a) Power analysis of $PdTe_2$ terahertz emission spectrum intensity according to Eq. (4) shows mixing of quadratic, linear, and cubic behavior at different frequencies. For almost all frequencies, linear dominates except toward zero frequency, where quadratic takes over. (b) A logarithmic plot of the coefficients of Eq. (4) shows the fitting finds either linear plus quadratic or linear plus cubic behavior at a given frequency. Linear and cubic contributions are found to dominate the 1.7–2.7 THz band where $PdTe_2$ emits greater intensities than the reference pulse, suggesting third-order processes are responsible for the observed spectral enhancement over reference at higher frequencies.

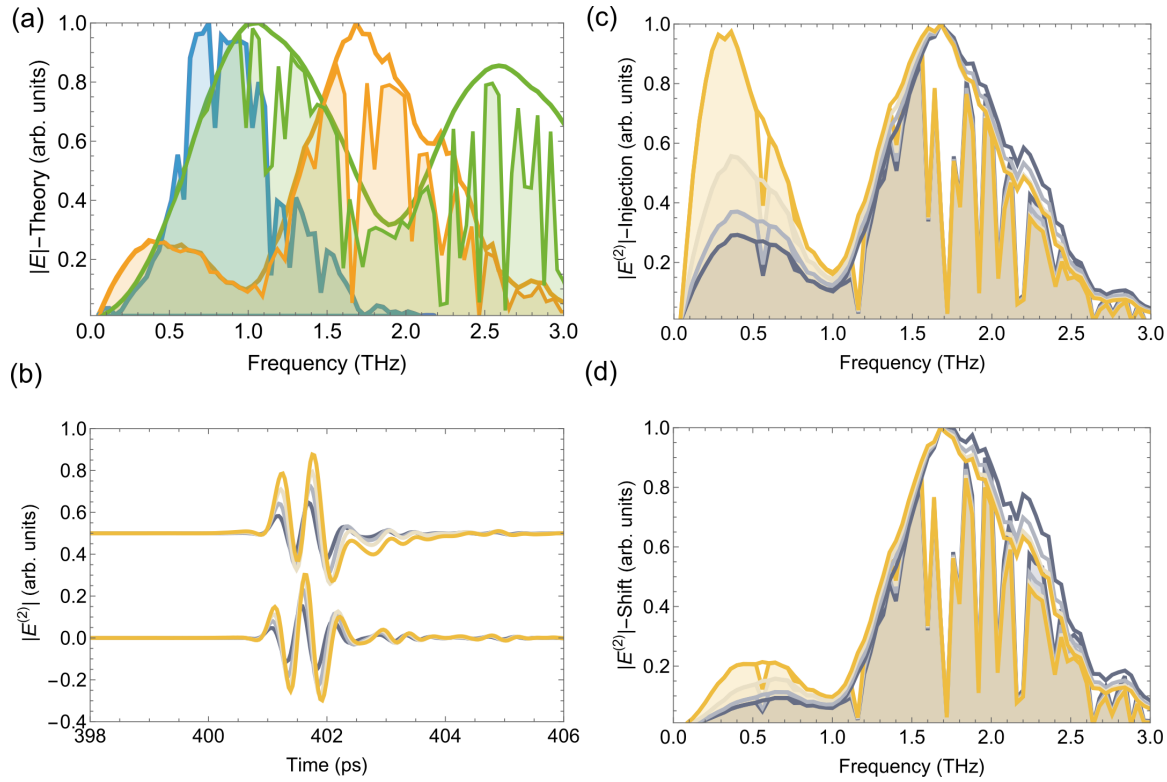


FIG. 6. (a) Second- (orange) and third-order (green) response spectra calculated according to Eq. (6) using the reference terahertz pulse (blue). Each spectrum is individually normalized by its peak intensity. The solid curves show the result of applying laboratory transmission and absorption to the theoretical spectra. (b) Time-dependent radiated pulses generated by injection (top) and shift (bottom) currents for increasing lifetimes $\tau_{\text{inj/sh}} = 0.05, 0.1, 0.2, 0.5$ ps are shown in the gray to yellow curves. The increasing lifetimes drive up the near-DC response of the injection current. The corresponding Fourier spectra normalized by their peak intensity are shown in (c) and (d), where the solid curves account for atmospheric absorption and transmission. Phenomenologically, the injection current spectra for τ_{inj} more closely matches the data in Fig. 5.

Fermi surface or intraband contributions to the Drude conductivity in quantum materials [57]. At these energy and timescales, it is more natural to dynamically relate the radiated, $E_{\text{rad}}(t)$, and incoming, $E_{\text{in}}(t)$, electric fields through the photocurrent $j(t)$ generated by the NLO conductivity. In Appendix C, we show this can be written as

$$\begin{aligned} j(t) &= \left[\sigma^{(1)} * E_{\text{in}} + \sigma^{(2)} * E_{\text{in}}^2 + \sigma^{(3)} * E_{\text{in}}^3\right](t), \\ E_{\text{rad}}(t) &\propto -\partial_t j(t; E_{\text{in}}(t)), \end{aligned} \tag{5}$$

where $*$ is the convolution operator, and $\sigma^{(n)}(t_1, \ldots, t_n)$ are the time-dependent nth-order nonlinear conductivities. Following our derivation in Appendix C, if the nonlinear response kernel $\sigma^{(n)}(\omega_1, \ldots, \omega_n)$ is constant over the incoming spectrum $E_{\text{in}}(\omega)$ then the nth nonlinear contribution to the radiated spectrum, $E_{\text{rad}}^{(n)}(t)$, is simply

$$E_{\text{rad}}^{(n)}(t) \approx -\sigma_0^{(n)} E_{\text{in}}(t)^{n-1} \partial_t E_{\text{in}}(t). \tag{6}$$

Here $\sigma_0^{(n)}$ is the nth-order NLO susceptibility strength, and we have suppressed the tensor nature of the NLO response; as for linearly polarized light, all components of $E_{\text{in}}(t)$ are in phase. Using Eq. (6) we calculate the theoretical second- and third-order emitted fields and present their Fourier spectra alongside $E_{\text{in}}(f)$ in Fig. 5. The theoretical spectrum indicates second- and third-order activity should be dominant for the same frequencies as determined by the power analysis in Fig. 5. However, the theory in Fig. 6 predicts a SHG peak at about 1.75 eV while the power analysis instead displays a peak closer to about 1.5 eV. This can be accounted for by the atmospheric (mostly water) absorption in the laboratory. The reference pulse can be seen to have a large absorption peak around 1.75 eV. To verify this, we performed direct measurement of our terahertz pulse in free space and then in a box with purged nitrogen atmosphere maintaining the same path length as our reflection geometry experiments to obtain the transmission spectrum of our laboratory (see Appendix E). We can then apply this transmission spectrum to the theoretical higher-order response, and see that the atmospherically adjusted theoretical second-order spectrum now peaks at about 1.5 eV in Fig. 6(a).

To obtain a greater understanding of the underlying excitation processes of the experimental observations, physically realistic nonlinear conductivity kernels have to be employed in the theoretical analysis. For example, in Appendix D we demonstrate that by properly employing the Drude conductivity for the linear response component we see that the *reflected* and incoming pulses are spectrally similar, and in fact become identical in the clean (i.e., long-scattering-time) limit. In the case of second-order response, we seek to elucidate why the peak values of the DC and SHG contributions to E_{rad} are comparable. The true $\sigma^{(2)}(\omega_1, \omega_2)$ function will not be spectrally flat due to resonant transi-

tions and excitation lifetimes. Consider the second-order shift and injection current response functions introduced by Braun *et al.* [58]:

$$\sigma^{(2)}_{\mathrm{inj}}(t-t_1,t-t_2)=\sigma_{\mathrm{inj}}\delta(t_1-t_2)\Theta(t-t_1)e^{-(t-t_1)/\tau_{\mathrm{inj}}}, \quad (7)$$

$$\sigma^{(2)}_{\mathrm{sh}}(t-t_1,t-t_2) = \sigma_{\mathrm{sh}}\delta(t_1-t_2)\left(\delta(t-t_2)-\Theta(t-t_1)\frac{e^{-(t-t_1)/\tau_{\mathrm{sh}}}}{\tau_{\mathrm{sh}}}\right). \quad (8)$$

In this approximation, only the intensity of the electric field $|E(t)|^2$ matters due to the δ-function constraint $t_1 = t_2$. The relaxation times and strengths of the injection and shift excitations are given respectively by $\tau_{\mathrm{inj/sh}}$ and $\sigma_{\mathrm{inj/sh}}$. We apply these kernels to our injected terahertz pulse and take the time derivative to generate the emitted pulses in Fig. 6(b). We consider relaxation times of $\tau_{\mathrm{inj/sh}} = 0.05$, 0.1, 0.2, and 0.5 ps to cover the orders of excitation timescales observable in terahertz spectroscopy [58]. The longer lifetimes translate into longer-lived second-order pulses, and correspondingly increase the weight of the near-DC peak in the corresponding Fourier spectra in Figs. 6(c) and 6(d). In the limit of a long shift current lifetime, $\tau_{\mathrm{sh}} \to \infty$, the shift current response kernel approaches $\sigma^{(2)}_{\mathrm{sh}}(t-t_1,t-t_2) \to \delta(t-t_1)\delta(t-t_2)$, which is equivalent to the simple theory approach discussed previously. This explains why the shift current and simple theory spectra in Figs. 6(a) and 6(d) appear similar for long lifetimes. On the other hand, the injection current is dominated by the low-frequency or DC response as the lifetime increases, suggesting that the second-order activity extracted in Fig. 5(b) originates from an injection current process with a lifetime on the order of 100 fs.

We note that while the shift and injection current kernels conceived by Braun *et al.* seemingly capture the behavior of the second-order spectra, at the terahertz energy scale excitations about the Fermi surface (including quantum geometric contributions) can play a role in the nonlinear terahertz response of a centrosymmetric material with topological surface states [14,59]. Additionally, photon drag effects can manifest at the terahertz scale [60,61]. The microscopic formulas for these various contributions have been determined in other works, and it has been found that in the semiclassical limit many of these responses take on the same dynamical functional behavior as formulated by Braun *et al.* (especially when the constraint $t_1 = t_2$ is applied) [11,62]. Future studies of $PdTe_2$ should thus combine microscopic Hamiltonian based calculations with transmission THz spectroscopy measurements in purged environments to isolate the different $\sigma^{(n)}_{ijk\ldots}$ tensor components, and investigate their precise origin.

V. CONCLUSION

We have studied the NLO responses of single-crystal $PdTe_2$ using visible (SHG and FWM) and terahertz spectroscopy. We conclude that second- and third-harmonic processes are clearly present in these disparate bands, indicating broadband nonlinear activity in $PdTe_2$ despite its inversion-symmetric crystal structure.

In the visible spectrum studies adheres to the surface point-group symmetry C_{3v} of $PdTe_2$, which is consistent with the single-crystal nature of the material. Moreover, despite the inversion symmetry of the bulk crystal, clear SHG was observed and was resonantly enhanced when the SHG energy coincided with the separation of topological surface state Dirac points. Such an enhancement between buried conduction- and valence-band Dirac points has previously been witnessed in topological insulator photogalvanic effect studies, and suggests $PdTe_2$ hosts a circular photogalvanic effect measurable in future studies [13].

In the terahertz spectroscopy studies, we found that linear response combined with third-harmonic generation is sufficiently strong to produce a relative increase in the emitted spectrum at higher frequencies. Given that third-harmonic generation is the sister process of fundamental enhancement, this suggests that $PdTe_2$ could be used for self-focusing and frequency upconversion in future terahertz-based studies. By studying the power dependence of our radiated spectrum, we were further able to extract both second- and third-order NLO processes, despite the broadband nature of the excitation pulse. Leveraging data on the transmission spectrum of our laboratory and careful application of nonlinear photocurrent theory, we found we could phenomenologically reproduce the experimental results using only the measured input pulse. To the best of our knowledge, the extraction of NLO activity in open atmosphere reflection geometry experiments is rarely conducted due to the challenges we overcame in this study. Our work lays the foundation for future terahertz reflection geometry experiments where transmission is not feasible, and provides a framework for studying NLO activity in broad spectra. Finally, the presence of SHG and near-DC terahertz peaks in the emitted spectra shows that $PdTe_2$ likely possesses decent low-energy photogalvanic or photon drag effects. This motivates future studies on photocurrent generation in $PdTe_2$ to identify terahertz nonlinear photocurrent generation and possible nonlinear Hall effects. Specifically, the dependence of the photocurrent on the helicity of the incoming optical excitation controlled through a quarter-wave plate could clarify the injection versus shift current nature of the low-frequency second-order response.

ACKNOWLEDGMENTS

The authors thank Elisabeth Schreiner and Bärbel Zimmermann for performing the TOF-SIMS measurements of the $PtSe_2$ crystal. G.J.d.C. would like to acknowledge funding from the U.S. Office of the Deputy Assistant Secretary of the Army for Defense Exports and Cooperation Engineering and Scientist Exchange Fellowship program. L.L. and A.H. were funded by the Deutsche Forschungsgemeinschaft (DFG, German Research Foundation), Grant No. 558231736. Z.S. was supported by ERC-CZ program (Project No. LL2101) from Ministry of Education Youth and Sports (MEYS) and by the project Advanced Functional Nanorobots (Registration No. CZ.02.1.01/0.0/0.0/15_003/0000444 financed by the EFRR). This research was supported by a Laboratory University Collaborative Initiative award provided by the Basic Research Office in the Office of the Under Secretary of Defense for Research and Engineering and by the Army Research Office and was accomplished under Cooperative Agreement No. W911NF2520010 (STEP-TWO). The views and conclu-

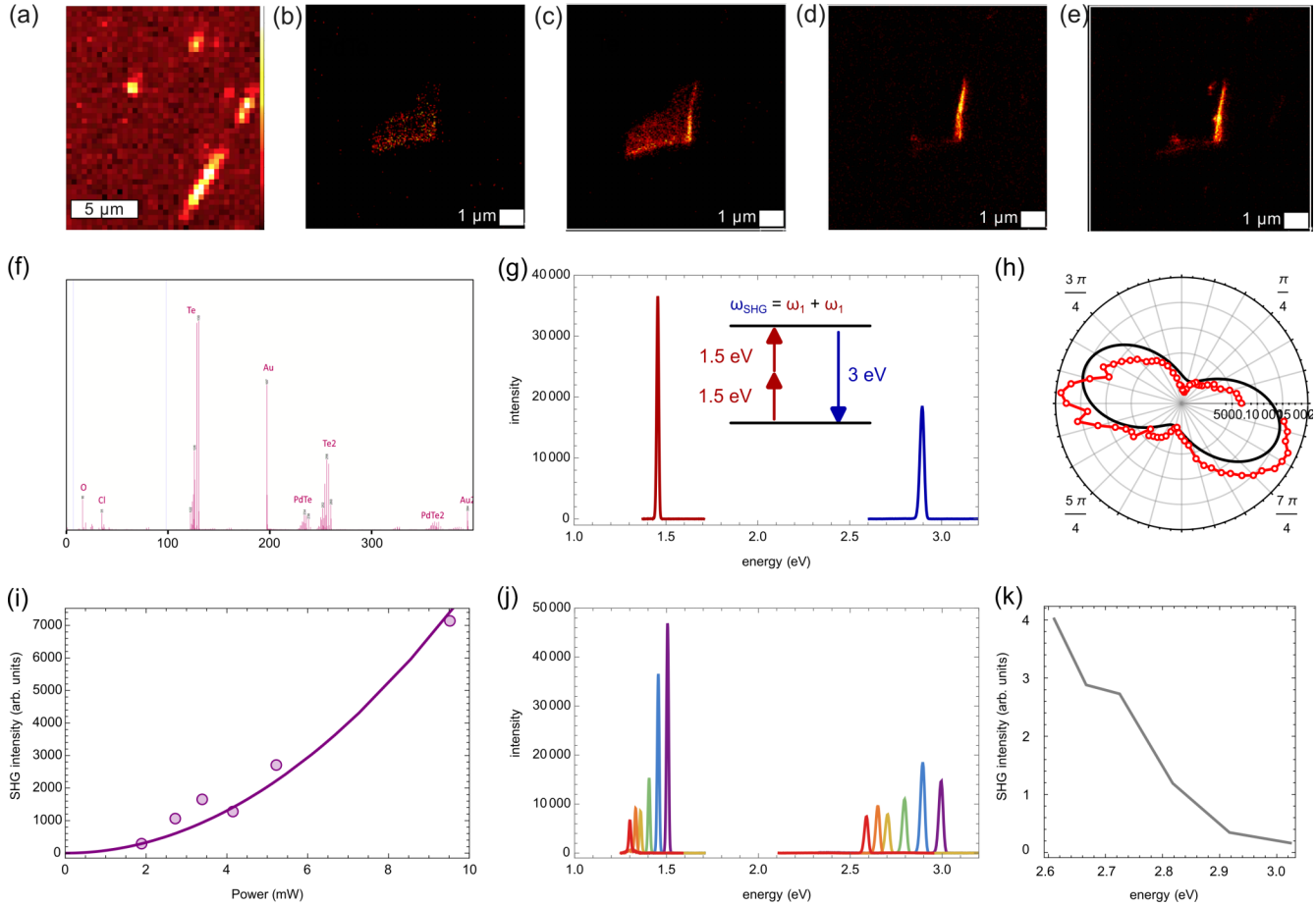


FIG. 7. (a) Spatial scan of the SHG intensity on the $PdTe_2$ crystal surface over a 14×16 μm^2 area. [(b)–(e)] Time-of-flight secondary ion mass spectroscopy (TOF-SIMS) intensity of detected sputtered molecular composition of an exfoliated $PdTe_2$ from the same bulk crystal showing additional clusters of chlorine and oxygen accumulation in single spots and along step edges in the $PdTe_2$. Scale bars are 1 μm. (f) Single TOF-SIMS spectrum showing detected impurities from the $PdTe_2$ crystal surface. (g) Optical second-harmonic generation at 3 eV in $PdTe_2$ stimulated by a 1.5-eV pulsed laser. (h) The symmetry of the polarization of the SHG response to varying the polarization of the 1.5-eV pulse and 3-eV emission by a half-wave plate is found to exhibit twofold symmetry which is inconsistent with the C_{3v} surface point group of $PdTe_2$ but points toward a symmetry reduction due to defects and step edges at the surface. (i) The power dependence of the SHG at 3 eV is shown to be quadratic in the pulse power, consistent with SHG scaling. (j) The input pulse wavelength is varied and (k) the resulting SHG intensity ratio to the square of the input intensity is plotted in gray. We note that while we can observe that these brighter spots and edges can have an order-of-magnitude-higher SHG intensity as compared to the bare $PdTe_2$ surface, we believe the overall SHG intensity to be dominated by the bigger area of bare $PdTe_2$ surface. However, in our terahertz measurements, the large spot size diameter of 300–500 μm makes these contributions indistinguishable.

sions contained in this document are those of the authors and should not be interpreted as representing the official policies, either expressed or implied, of the Army Research Office or the U.S. Government. The U.S. Government is authorized to reproduce and distribute reprints for Government purposes notwithstanding any copyright notation thereon. We thank dtec.bw—Digitalization and Technology Research Center of the Bundeswehr for support (project VITAL-SENSE). dtec.bw is funded via the German Recovery and Resilience Plan by the European Union (NextGenerationEU)

DATA AVAILABILITY

The data that support the findings of this article are not publicly available because of legal restrictions preventing unrestricted public distribution. The data are available from the authors upon reasonable request.

APPENDIX A: SECOND-HARMONIC GENERATION AREA SCAN AND DEFECTS

Measurements realized in the bright spot area and the analyses of the second-harmonic signals generated by these regions in the sample of $PdTe_2$ are shown in Fig. 7.

APPENDIX B: DETERMINING SECOND- AND THIRD-ORDER NONLINEAR SUSCEPTIBILITIES ($\chi^{(2)}$ AND $\chi^{(3)}$)

To determine the nonlinear optical susceptibilities of $PdTe_2$, we employed a comparative method using well-

TABLE I. Second-order nonlinear susceptibility of various monolayers (ML) and heterobilayers (HBL) of 2D materials.

Material	λ_F (nm)	$\chi^{(2)}(2\omega)$ (nm^2/V)	Ref.
ML WS_2	832	5.9	[64]
ML MoS_2	810	3.3	[65]
ML $MoSe_2$	≈800	1.7	[66]
$PdTe_2$	820	5.0	Our work
HBL $MoSe_2/WS_2$	1030	0.0091	[67]
ML WSe_2	1550	0.07	[68]
Graphene on Au	780	1.4	[69]

characterized reference materials measured under identical experimental conditions similar to the work of Malard *et al.* [36] and Lafeta *et al.* [47]. Both the second- and third-order responses were collected in a backscattering geometry using the same 0.95 numerical aperture (NA) air objective, ensuring that the focal volume, collection efficiency, and Fresnel factors are directly comparable between samples. The corresponding susceptibility can then be estimated following the derivation of Boyd via [40]

$$\chi^{(2)}_{\text{surf}}(R, n_S(\omega), n_S(2\omega)) = 2.8\times10^{-18}\sqrt{\frac{0.62\,R}{\left|\frac{2n_S(2\omega)}{1+n_S(2\omega)}\right|^2\left|\frac{2}{1+n_S(\omega)}\right|^4}}\ \text{m}^2/\text{V}, \tag{B1}$$

where $R=\frac{I_{PdTe_2}(2\omega)}{I_{\text{quartz}}(2\omega)}$ (the measured SHG intensity ratio), $n_S(\omega)$ is the refractive index of $PdTe_2$ at the fundamental wavelength [63], and $n_S(2\omega)$ is the refractive index of $PdTe_2$ at the SHG wavelength [63]. All other constants [crystalline quartz second-order susceptibility ($\chi^{(2)}_{\text{CQ}}=0.8\times10^{-12}$ m/V [39]), confocal interaction length, and Fresnel factors for quartz] are already absorbed into the numerical prefactors 2.8×10^{-18} and 0.62.

The optical second-order nonlinear surface susceptibility that we report is similar to, and in some cases surpasses, the second-order nonlinear susceptibility sheet of symmetry-broken two-dimensional materials, as shown in Table I.

Unlike $\chi^{(2)}$, bulk inversion-symmetric materials have nonzero $\chi^{(3)}$ tensor elements, and so the third-order response will be generated by multiple layers. The effective third-order susceptibility is given by the equation $\chi^{(3)}_{\text{eff}}=\chi^{(3)}_{\text{sheet}}/t$ and is extracted by comparing the FWM signal of $PdTe_2$ bulk with that of a 0.11-mm fused-quartz reference, whose susceptibility $\chi^{(3)}_{\text{FQ}}=2.0\times10^{-22}$ m^2/V^2 is well established [39]. For the FWM process $2\omega_1-\omega_2=\omega_{\text{FWM}}$ with $\lambda_1=780$ nm, $\lambda_2=930$ nm, and $\lambda_{\text{FWM}}\approx670$ nm, the resulting expression is

$$\chi^{(3)}_{PdTe_2}(R, n_1, n_2, n_F) = 2.0\times10^{-22}\frac{1.45}{n_1}\sqrt{\frac{0.414\,R}{\left|\frac{2n_F}{1+n_F}\right|^2\left|\frac{2}{1+n_1}\right|^4\left|\frac{2}{1+n_2}\right|^2}}\ \text{m}^2/\text{V}^2. \tag{B2}$$

where $R=I^{\text{FWM}}_{PdTe_2}/I^{\text{FWM}}_{\text{FS}}$ (the measured FWM intensity ratio), $n_1=n_{PdTe_2}(780\,\text{nm})$, $n_2=n_{PdTe_2}(930\,\text{nm})$, and $n_F=n_{PdTe_2}(670\,\text{nm})$, the refractive indices of $PdTe_2$ at the respective wavelengths [63]. The numerical constants incorporate the fused quartz refractive index, its known $\chi^{(3)}_{\text{FQ}}=2.0\times10^{-22}$ m^2/V^2, and the fixed Fresnel factors for backscattering.

Using the experimentally measured ratio $R\approx42$ and the refractive indices $n_1=2.2$, $n_2=2.6$, and $n_F=1.7$ [63], we obtain

$$\chi^{(3)}_{PdTe_2}\approx2\times10^{-21}\ \text{m}^2/\text{V}^2. \tag{B3}$$

This value is between one and two orders of magnitude lower than third-order susceptibilities reported previously for transition metal dichalcogenides such as $MoTe_2$ [70], group-VI compounds [39,70,71], and graphene [47,70], confirming that $PdTe_2$ exhibits a comparable or lower third-order nonlinear optical response when compared to literature results using approximately the same wavelength (but occasionally different spectroscopy studies such as THG).

APPENDIX C: NONLINEAR OPTICAL RESPONSE FUNCTIONS AND INSTANT INTERACTIONS

The temporal representations of linear, second-order, and third-order photocurrents are given by [40]

$$j^{(1)}(t)=\int_{-\infty}^{\infty}E(t_1)\sigma^{(1)}(t-t_1)dt_1, \tag{C1a}$$

$$j^{(2)}(t)=\int_{-\infty}^{\infty}E(t_1)E(t_2)\sigma^{(2)}(t-t_1,t-t_2)dt_1dt_2, \tag{C1b}$$

$$j^{(3)}(t)=\int_{-\infty}^{\infty}E(t_1)E(t_2)E(t_3)\times\sigma^{(3)}(t-t_1,t-t_2,t-t_3)dt_1dt_2dt_3. \tag{C1c}$$

In frequency space there is always one less integral because of the convolution theorem:

$$j^{(1)}(\Omega)=E(\Omega)\sigma^{(1)}(\Omega), \tag{C2a}$$

$$j^{(2)}(\Omega)=\int_{-\infty}^{\infty}E(\Omega-\omega_1)E(\omega_1)\sigma^{(2)}(\Omega-\omega_1,\omega_1)d\omega_1, \tag{C2b}$$

$$j^{(3)}(\Omega)=\int_{-\infty}^{\infty}E(\Omega-\omega_1-\omega_2)E(\omega_1)E(\omega_2)\times\sigma^{(3)}(\Omega-\omega_1-\omega_2,\omega_1,\omega_2)d\omega_1d\omega_2. \tag{C2c}$$

We have absorbed normalization constants into our definitions of $\sigma^{(n)}$ and suppressed tensor indices as for now we are only concerned with time and frequency structures.

Within this paper, we study the electric field emitted by $PdTe_2$ after excitation with a terahertz pulse. If we assume the emitted electric field is generated by the acceleration and deceleration of charge carriers, then the terahertz field radiated from the sample and measured at location $\boldsymbol{r}$ and time t can be expressed as [72]

$$\boldsymbol{E}_{\text{rad}}(\boldsymbol{r},t)=-\frac{1}{4\pi\epsilon_0c^2}\int d\boldsymbol{r}'\frac{1}{|\boldsymbol{r}-\boldsymbol{r}'|}\partial_t\boldsymbol{j}(\boldsymbol{r}',t-|\boldsymbol{r}-\boldsymbol{r}'|/c). \tag{C3}$$

Equation (C3) implies that the dynamics of the measured terahertz field are dictated by the NLO susceptibility tensors

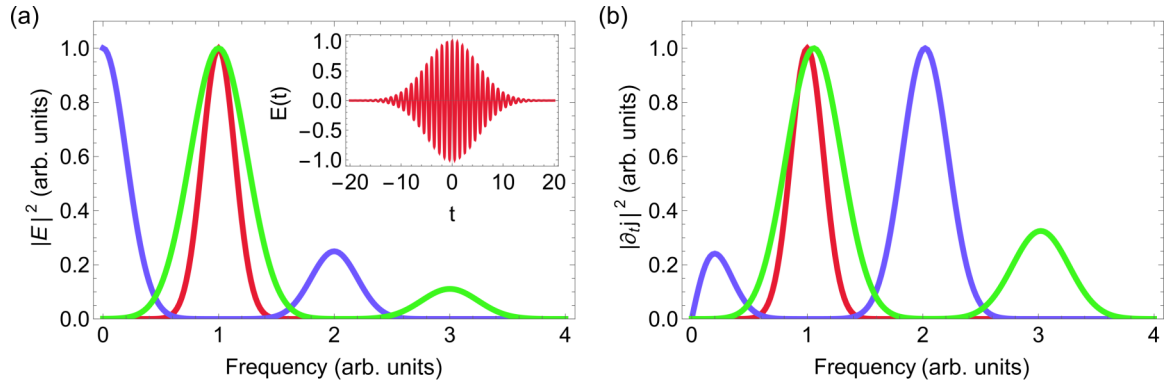


FIG. 8. Frequency spectrum plots of $E^{(n)}_{\text{rad}}$ intensities according to (a) the standard polarization framework $E^{(n)}_{\text{rad}} \equiv P^{(n)}(\Omega) \sim |\chi^{(n)}_0 \int dt e^{i\Omega t} E(t)^n|$ and (b) the radiative photocurrent framework in Eq. (C7). The incoming spectrum is shown in red, and second- and third-order response spectra are shown in blue and green, respectively. The inset in both cases is the incoming monochrome pulse. The primary differences due to the extra Ω in Eq. (C7) are the elimination of the DC component, the shifted relative peak height, and the peak positions.

$\chi^{(n)}(t-t_1,\ldots,t-t_n)$ which are defined by

$$\chi^{(n)}(t-t_1,\ldots,t-t_n) = -\frac{\partial}{\partial t}\sigma^{(n)}(t-t_1,\ldots,t-t_n). \quad \text{(C4)}$$

Given that 1-THz frequency light has energy of 4.14 meV, the excitations involved in terahertz spectroscopy are small on the scale of the $PdTe_2$ band structure shown in Fig. 1. This suggests that the semiclassical or low-excitation-energy limits of NLO tensor theory can account for our observed phenomena. In this limit, as long as there is no resonant excitation, the Fourier representation of the NLO functions $\sigma^{(n)}(\omega_1,\ldots,\omega_n)$ will depend on frequencies through terms such as $1/(\omega_n + i\gamma)$ where $\gamma = 1/\tau_s$ is the inverse lifetime of the carrier [4,62,73]. Provided γ is large compared to the frequencies ω for which $E(\omega)$ is nonzero, we can safely approximate constant spectral behavior, $\sigma^{(n)}(\omega_1,\ldots,\omega_n) \approx$ const. In this case, $\sigma^{(n)}(t-t_1,\ldots,t-t_n) = \sigma^{(n)}_0 \delta(t-t_1)\cdots\delta(t-t_n)$. This behavior reflects that, with respect to the timescales of the measurement, we expect the electric field to instantaneously interact with itself with some weight $\sigma^{(n)}_0$. Deviations from this base case should demonstrate a retarded response of the material owing to finite lifetimes. Then the NLO current is simply

$$j^{(n)}(t) = \sigma^{(n)}_0 E(t)^n, \quad \text{(C5)}$$

and the nth NLO component of the radiated field in time and Fourier space is given by

$$E^{(n)}_{\text{rad}}(t) = -n\sigma^{(n)}_0 E(t)^{n-1}\partial_t E(t), \quad \text{(C6)}$$

$$\left|E^{(n)}_{\text{rad}}(\Omega)\right| = \left|n\sigma^{(n)}_0 \int dt e^{i\Omega t}\Omega E(t)^n\right|. \quad \text{(C7)}$$

As an example, we can calculate $E^{(2)}_{\text{rad}}(\Omega)$ and $E^{(3)}_{\text{rad}}(\Omega)$ according to Eq. (C7) in response to a monochrome pulse centered at a frequency of 1. We present these in Fig. 8 and compare them to the traditional polarization formalism of higher-harmonic generation, where the NLO response tensor $\chi^{(n)}$ is assumed to be spectrally independent and so $E^{(n)}_{\text{rad}}(\Omega) \equiv P^{(n)}(\Omega) \sim |\chi^{(n)}_0 \int dt e^{i\Omega t} E(t)^n|$.

APPENDIX D: FINITE LIFETIME IN LINEAR RESPONSE

It is interesting to consider the impact of lifetime on the linear response to the terahertz pulse. Motivated by Refs. [54,74], consider the linear response current:

$$j(t) = \int_{-\infty}^{\infty} E(t_1)\sigma(t-t_1)dt_1. \quad \text{(D1)}$$

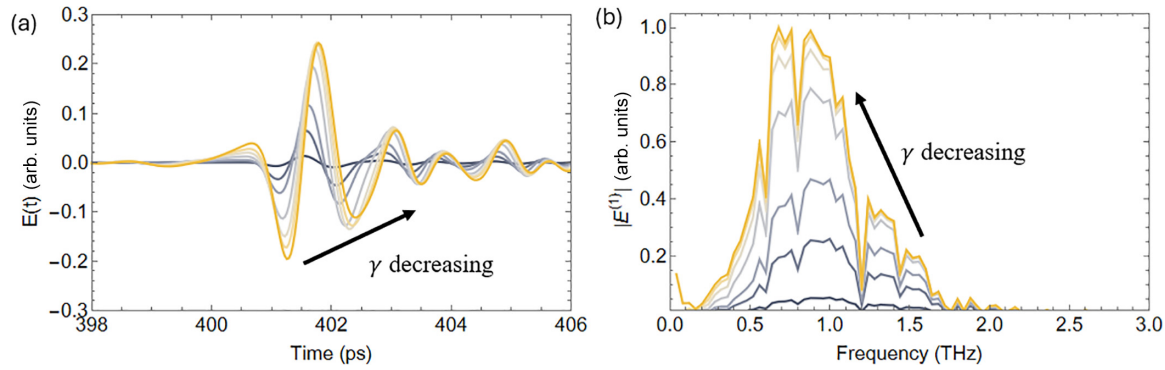


FIG. 9. Effects of carrier dynamics on the radiated electric field with $\gamma = 1/\tau_s$ for τ_s ranging from 0 to 1 ps in linear response. The final yellow curves correspond to the injected terahertz pulse used to compute the first-order response according to Eq. (D6).

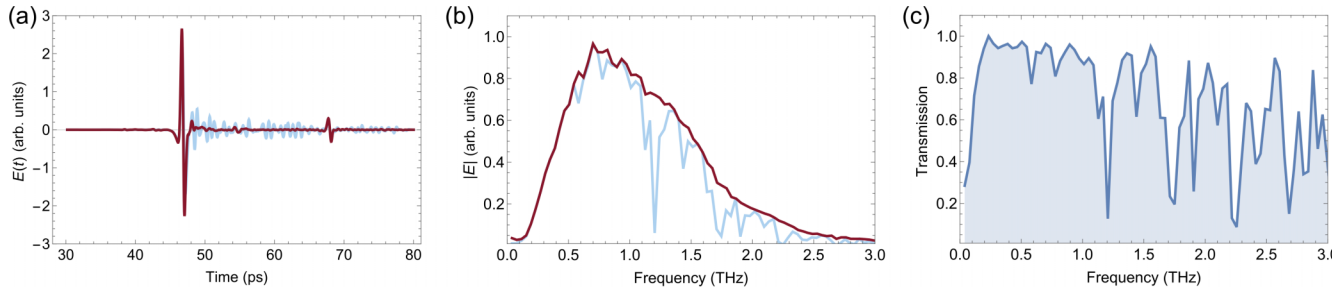


FIG. 10. (a) Terahertz waveform collected in purged (red) and atmospheric (blue) conditions to compute the overall transmission spectrum of the laboratory. The corresponding spectra and resulting transmission are shown in (b) and (c).

For the Drude model, we have the well-known form of conductivity:

$$\sigma(t) = \frac{ne^2}{m}\Theta(t)e^{-\gamma t}, \tag{D2}$$

$$\sigma(\omega) = \frac{ne^2}{m}\frac{-i}{\omega + i\gamma}, \tag{D3}$$

where γ is the scattering rate or inverse lifetime. Multiple NLO responses such as electrical polarization, magnetization, and electric quadrupole densities can underlie the current $j(t)$, further complicating the expression for $\sigma(t)$, but for now we will limit ourselves to a carrier dynamics framework [1]. Following the discussion in Appendix C, we relate the photocurrent to the electric field simply through $-\partial_t j(t) \sim E_{\text{rad}}(t)$:

$$-\partial_t j(t) = -\int_{-\infty}^{\infty} E(t_1)\partial_t\sigma(t - t_1)dt_1. \tag{D4}$$

Then we have

$$\chi(\tau) \equiv -\partial_\tau\sigma(\tau) = \frac{ne^2}{m}(-\delta(\tau) + \gamma e^{-\gamma\tau}\Theta(\tau)). \tag{D5}$$

We have neglected the first instance of $e^{-\gamma\tau}$ as the δ function forces $\tau = 0$. Temporally the radiated electric field thus has an instant response given by a first time, and a time-lagged response accounting for carrier dynamics. In Ref. [54] a similar expression is derived where effects such as hot electrons are accounted for through more complicated time-dependent γ. In a short-lifetime approximation, $\gamma \to \infty$ and the term $\gamma e^{\gamma\tau} \to \delta(\tau)$ for $\tau \leqslant 0$, which ultimately eliminates the response, while for longer lifetimes $e^{-\gamma\tau} \to 0$, and the response function is just proportional to $\delta(\tau)$. This behavior is summarized in Fig. 9, where we numerically compute

$$E_{\text{rad}}(t) \sim -\int_{-\infty}^{\infty} E(t - t_1)\chi(t_1)dt_1, \tag{D6}$$

which allows us to limit the range of integration to $|t_1| < 5/\gamma$ and capture 0.993 of the integral kernel. As $\tau_s \to \infty$ or $\gamma \to 0$, the reflected pulse retards and sharpens spectrally. The final yellow curves in Figs. 9(a) and 9(b) correspond to the injected pulse, showing that in the clean limit the Drude model results in perfect reflection. In frequency space this conclusion could also have been reached by noting that under the Fourier transform $\partial_t\sigma(t) \to i\omega\sigma(\omega)$ and when $\gamma \to 0$ one has $\omega\sigma(\omega) \to$ const, so then $E_{\text{rad}}(\omega) \propto E_{\text{in}}(\omega)$.

APPENDIX E: LABORATORY ABSORPTION AND TRANSMISSION

The transmission spectrum of our laboratory environment was determined by measuring our emitters Terahertz waveform in both a purged and atmospheric conditions. The ratio of the corresponding spectra determines the transmission spectrum, and the data are collectively plotted in Fig. 10.

[1] J. Orenstein, J. E. Moore, T. Morimoto, D. H. Torchinsky, J. W. Harter, and D. Hsieh, Topology and symmetry of quantum materials via nonlinear optical responses, Annu. Rev. Condens. Matter Phys. **12**, 247 (2021).
[2] J. Shi *et al.*, Giant room-temperature nonlinearities in a monolayer Janus topological semiconductor, Nat. Commun. **14**, 4953 (2023).
[3] I. Sodemann and L. Fu, Quantum nonlinear Hall effect induced by Berry curvature dipole in time-reversal invariant materials, Phys. Rev. Lett. **115**, 216806 (2015).
[4] Y. Onishi and L. Fu, High-efficiency energy harvesting based on a nonlinear Hall rectifier, Phys. Rev. B **110**, 075122 (2024).
[5] H. Wu, Y. Wang, Y. Xu, P. K. Sivakumar, C. Pasco, U. Filippozzi, S. S. P. Parkin, Y.-J. Zeng, T. McQueen, and M. N. Ali, The field-free Josephson diode in a van der Waals heterostructure, Nature (London) **604**, 653 (2022).
[6] P. K. Sivakumar, M. T. Ahari, J.-K. Kim, Y. Wu, A. Dixit, G. J. de Coster, A. K. Pandeya, M. J. Gilbert, and S. S. P. Parkin, Long-range phase coherence and tunable second order φ_0-Josephson effect in a Dirac semimetal 1T-$PtTe_2$, Commun. Phys. **7**, 354 (2024).
[7] Y. Liu and Q. Shao, Two-dimensional materials for energy-efficient spin-orbit torque devices, ACS Nano **14**, 9389 (2020).
[8] J. Hidding, K. Mërtiri, F. Mujid, C. Liang, J. Park, and M. H. D. Guimarães, Role of self-torques in transition metal dichalcogenide/ferromagnet bilayers, Phys. Rev. B **108**, 064419 (2023).
[9] B. C. Connelly, P. J. Taylor, and G. J. de Coster, Emergence of threefold symmetric helical photocurrents in epitaxial low

twinned Bi_2Se_3, Proc. Natl. Acad. Sci. USA **121**, e2307425121 (2024).

[10] H. Plank *et al.*, Infrared/terahertz spectra of the photogalvanic effect in (Bi, Sb)Te based three-dimensional topological insulators, Phys. Rev. Mater. **2**, 024202 (2018).

[11] Y.-M. Xie and N. Nagaosa, Photon-drag photovoltaic effects and quantum geometric nature, Proc. Natl. Acad. Sci. USA **122**, e2424294122 (2025).

[12] M. Hemmat *et al.*, Layer-controlled nonlinear terahertz valleytronics in two-dimensional semimetal and semiconductor $PtSe_2$, InfoMat **5**, e12468 (2023).

[13] Y. Pan *et al.*, Helicity dependent photocurrent in electrically gated $(Bi_{1-x}Sb_x)_2Te_3$ thin films, Nat. Commun. **8**, 1037 (2017).

[14] F. Hu, P. Zhao, L. Yang, S. Zhao, J. Lei, W. Li, J. Lai, Z. Yu, H. Park, C. Wong, R. Sharma, G. Eda, S. A. Yang, X. Xu, F. Wang, and H. Yang, Ultrabroadband nonlinear Hall rectifier using SnTe, Nat. Nanotechnol. **20**, 1588 (2025).

[15] Y. Zhang and L. Fu, Terahertz detection based on nonlinear Hall effect without magnetic field, Proc. Natl. Acad. Sci. USA **118**, e2100736118 (2021).

[16] C. Yim, K. Lee, N. McEvoy, M. O'Brien, S. Riazimehr, N. C. Berner, C. P. Cullen, J. Kotakoski, J. C. Meyer, M. C. Lemme, and G. S. Duesberg, High-performance hybrid electronic devices from layered $PtSe_2$ films grown at low temperature, ACS Nano **10**, 9550 (2016).

[17] J. B. McManus, D. V. Horvath, M. P. Browne, C. P. Cullen, G. Cunningham, T. Hallam, K. Zhussupbekov, D. Mullarkey, C. Ó Coileáin, I. V. Shvets, M. Pumera, G. S. Duesberg, and N. McEvoy, Low-temperature synthesis and electrocatalytic application of large-area $PtTe_2$ thin films, Nanotechnology **31**, 375601 (2020).

[18] W. Zheng *et al.*, Detailed study of the Fermi surfaces of the type-II Dirac semimetallic candidates XTe_2 (X = Pd, Pt), Phys. Rev. B **97**, 235154 (2018).

[19] O. J. Clark *et al.*, Fermiology and superconductivity of topological surface states in $PdTe_2$, Phys. Rev. Lett. **120**, 156401 (2018).

[20] M. N. Ali *et al.*, Galvanomagnetic properties of the putative type-II Dirac semimetal $PtTe_2$, Sci. Rep. **8**, 15383 (2018).

[21] Y. Wang *et al.*, De Hass-van Alphen and magnetoresistance reveal predominantly single-band transport behavior in $PdTe_2$, Sci. Rep. **6**, 31554 (2016).

[22] K. Zhussupbekov, L. Ansari, J. B. McManus, A. Zhussupbekova, I. V. Shvets, G. S. Duesberg, P. K. Hurley, F. Gity, C. Coileáin, and N. McEvoy, Imaging and identification of point defects in $PtTe_2$, npj 2D Mater. Appl. **5**, 14 (2021).

[23] M. K. Lin, R. A. B. Villaos, J. A. Hlevyak, P. Chen, R.-Y. Liu, C.-H. Hsu, J. Avila, S.-K. Mo, F.-C. Chuang, and T.-C. Chiang, Dimensionality-mediated semimetal-semiconductor transition in ultrathin $PtSe_2$ films, Phys. Rev. Lett. **124**, 036402 (2020).

[24] Q. Gao *et al.*, Layer-dependent band gaps of platinum dichalcogenides, ACS Nano **15**, 13249 (2021).

[25] Z. Huang *et al.*, Crossover from 2D metal to 3D Dirac semimetal in metallic $PtTe_2$ films, Mater. Today Phys. **11**, 100161 (2019).

[26] S. M. Faizanuddin, C.-H. Chien, Y.-J. Chan, S.-T. Liu, C.-N. Kuo, C. S. Lue, and Y.-C. Wen, Surface second harmonic generation from topological Dirac semimetal $PdTe_2$, arXiv:2308.09053.

[27] G. Wang, K. Wang, N. McEvoy, Z. Bai, C. P. Cullen, C. N. Murphy, J. B. McManus, J. J. Magan, C. M. Smith, G. S. Duesberg, I. Kaminer, J. Wang, and W. J. Blau, Ultrafast carrier dynamics and bandgap renormalization in layered $PtSe_2$, Small **15**, 1902728 (2019).

[28] H. Wang, C. Zhang, and F. Rana, Surface recombination limited lifetimes of photoexcited carriers in few-layer transition metal dichalcogenide MoS_2, Nano Lett. **15**, 8204 (2015).

[29] L. Chu, Z. Li, H. Zhu, H. Lv, and F. Chen, Intense second-harmonic generation in two-dimensional $PtSe_2$, Nanophotonics **13**, 3457 (2024).

[30] C. Guo *et al.*, Anisotropic ultrasensitive $PdTe_2$-based phototransistor for room-temperature long-wavelength detection, Sci. Adv. **6**, eabb6500 (2020).

[31] C. Yim, V. Passi, M. C. Lemme, G. S. Duesberg, C. Ó Coileáin, E. Pallecchi, D. Fadil, and N. McEvoy, Electrical devices from top-down structured platinum diselenide films, npj 2D Mater. Appl. **2**, 5 (2018).

[32] Z. Peng, X. Chen, Y. Fan, D. J. Srolovitz, and D. Lei, Strain engineering of 2D semiconductors and graphene: From strain fields to band-structure tuning and photonic applications, Light: Sci. Appl. **9**, 190 (2020).

[33] X. Ge, X. Zhou, D. Sun, and X. Chen, First-principles study of structural and electronic properties of monolayer PtX_2 and Janus PtXY (X, Y = S, Se, and Te) via strain engineering, ACS Omega **8**, 5715 (2023).

[34] M. Cai *et al.*, Giant room-temperature terahertz photothermoelectric response mediated by hot carriers at the metal-semimetal interfaces, Sci. Adv. **11**, eadv0768 (2025).

[35] S. Heiserer *et al.*, Impact of strain in free-standing $PtSe_2$ in scalable 2D MEMS, Adv. Mater. **37**, e12564 (2025).

[36] L. M. Malard, T. V. Alencar, A. P. M. Barboza, K. F. Mak, and A. M. de Paula, Observation of intense second harmonic generation from MoS_2 atomic crystals, Phys. Rev. B **87**, 201401(R) (2013).

[37] Y. Li, Y. Rao, K. F. Mak, Y. You, S. Wang, C. R. Dean, and T. F. Heinz, Probing symmetry properties of few-layer MoS_2 and h-BN by optical second-harmonic generation, Nano Lett. **13**, 3329 (2013).

[38] L. Lafeta, S. Hartmann, B. Rosa, S. Reitzenstein, L. M. Malard, and A. Hartschuh, Probing noncentrosymmetric 2D materials by Fourier space second harmonic imaging, ACS Photonics **12**, 357 (2025).

[39] L. Lafeta *et al.*, Second- and third-order optical susceptibilities across excitons states in 2D monolayer transition metal dichalcogenides, 2D Mater. **8**, 035010 (2021).

[40] R. W. Boyd, *Nonlinear Optics*, 3rd ed. (Academic Press, Burlington, 2008).

[41] D. Hsieh, J. W. McIver, D. H. Torchinsky, D. R. Gardner, Y. S. Lee, and N. Gedik, Nonlinear optical probe of tunable surface electrons on a topological insulator, Phys. Rev. Lett. **106**, 057401 (2011).

[42] J. W. McIver, D. Hsieh, S. G. Drapcho, D. H. Torchinsky, D. R. Gardner, Y. S. Lee, and N. Gedik, Theoretical and experimental study of second harmonic generation from the surface of the topological insulator Bi_2Se_3, Phys. Rev. B **86**, 035327 (2012).

[43] Y. R. Shen, *The Principles of Nonlinear Optics* (John Wiley & Sons, New York, 1984).
[44] J. Yu *et al.*, Giant nonlinear optical activity in two-dimensional palladium diselenide, Nat. Commun. **12**, 1080 (2021).
[45] A. Virga *et al.*, Coherent anti-Stokes Raman spectroscopy of single and multi-layer graphene, Nat. Commun. **10**, 3658 (2019).
[46] G. Gordeev, L. Lafeta, B. S. Flavel, A. Jorio, and L. M. Malard, Excitonic resonances in coherent anti-Stokes Raman scattering from single-walled carbon nanotubes, J. Phys. Chem. C **127**, 20438 (2023).
[47] L. Lafeta *et al.*, Anomalous nonlinear optical response of graphene near phonon resonances, Nano Lett. **17**, 3447 (2017).
[48] L. Lange *et al.*, Ultrafast phase-control of the nonlinear optical response of 2D semiconductors, ACS Photonics **11**, 3112 (2024).
[49] X. Wen, Z. Gong, and D. Li, Nonlinear optics of two-dimensional transition metal dichalcogenides, InfoMat **1**, 317 (2019).
[50] A. Autere, H. Jussila, Y. Dai, Y. Wang, H. Lipsanen, and Z. Sun, Nonlinear optics with 2D layered materials, Adv. Mater. **30**, 1705963 (2018).
[51] M. S. Mrudul and G. Dixit, High-harmonic generation from monolayer and bilayer graphene, Phys. Rev. B **103**, 094308 (2021).
[52] W. Mao, A. Rubio, and S. A. Sato, Enhancement of high-order harmonic generation in graphene by mid-infrared and terahertz fields, Phys. Rev. B **109**, 045421 (2024).
[53] S. A. Mikhailov, Quantum theory of third-harmonic generation in graphene, Phys. Rev. B **90**, 241301(R) (2014).
[54] H. A. Hafez *et al.*, Extremely efficient terahertz high-harmonic generation in graphene by hot Dirac fermions, Nature (London) **561**, 507 (2018).
[55] K.-J. Tielrooij *et al.*, Milliwatt terahertz harmonic generation from topological insulator metamaterials, Light: Sci. Appl. **11**, 315 (2022).
[56] G. Soavi *et al.*, Broadband, electrically tunable third-harmonic generation in graphene, Nat. Nanotechnol. **13**, 583 (2018).
[57] L. Wu, M. Brahlek, R. Valdés Aguilar, A. V. Stier, C. M. Morris, Y. Lubashevsky, L. S. Bilbro, N. Bansal, S. Oh, and N. P. Armitage, A sudden collapse in the transport lifetime across the topological phase transition in $(Bi_{1-x}In_x)_2Se_3$, Nat. Phys. **9**, 410 (2013).
[58] L. Braun *et al.*, Ultrafast photocurrents at the surface of the three-dimensional topological insulator Bi_2Se_3, Nat. Commun. **7**, 13259 (2016).
[59] J. Stensberg, X. Han, Z. Ni, X. Yao, X. Yuan, D. Mallick, A. Gandhi, S. Oh, and L. Wu, Observation of terahertz second harmonic generation from Dirac surface states in the topological insulator Bi_2Se_3, Phys. Rev. B **109**, 245112 (2024).
[60] L. Cheng, Y. Xiong, L. Kang, Y. Gao, Q. Chang, M. Chen, J. Qi, H. Yang, Z. Liu, J. C. W. Song, and E. E. M. Chia, Giant photon momentum locked THz emission in a centrosymmetric Dirac semimetal, Sci. Adv. **9**, eadd7856 (2023).
[61] H. Plank, L. E. Golub, S. Bauer, V. V. Bel'kov, T. Herrmann, P. Olbrich, M. Eschbach, L. Plucinski, C. M. Schneider, J. Kampmeier, M. Lanius, G. Mussler, D. Grützmacher, and S. D. Ganichev, Photon drag effect in $(Bi_{1-x}Sb_x)_2Te_3$ three-dimensional topological insulators, Phys. Rev. B **93**, 125434 (2016).
[62] D. E. Parker, T. Morimoto, J. Orenstein, and J. E. Moore, Diagrammatic approach to nonlinear optical response with application to Weyl semimetals, Phys. Rev. B **99**, 045121 (2019).
[63] H. Chen, C. Xie, X. Zhong, Y. Liang, W. Yang, C. Wu, and L. Luo, A quasi-2D perovskite antireflection coating to boost the performance of multilayered $PdTe_2$/Ge heterostructure-based near-infrared photodetectors, J. Mater. Chem. C **10**, 6025 (2022).
[64] C. Janisch, Y. Wang, D. Ma, N. Mehta, A. L. Elías, N. Perea-López, M. Terrones, V. Crespi, and Z. Liu, Extraordinary second harmonic generation in tungsten disulfide monolayers, Sci. Rep. **4**, 5530 (2014).
[65] N. Kumar, S. Najmaei, Q. Cui, F. Ceballos, P. M. Ajayan, J. Lou, and H. Zhao, Second harmonic microscopy of monolayer MoS_2, Phys. Rev. B **87**, 161403(R) (2013).
[66] S. Puri, S. Patel, J. L. Cabellos, L. E. Rosas-Hernandez, K. Reynolds, H. O. H. Churchill, S. Barraza-Lopez, B. S. Mendoza, and H. Nakamura, Substrate interference and strain in the second-harmonic generation from $MoSe_2$ monolayers, Nano Lett. **24**, 13061 (2024).
[67] Z. Zhu, T. Yoo, K. Shaikh, A. C. Johnson, Q. Li, F. Liu, H. Deng, and Y. Kobayashi, Determining the complex second-order optical susceptibility in macroscale van der Waals heterobilayers, J. Chem. Phys. **163**, 174707 (2025).
[68] H. G. Rosa, H. Y. Wei, I. Verzhbitskiy, M. J. F. L. Rodrigues, T. Taniguchi, K. Watanabe, G. Eda, V. M. Pereira, and J. C. V. Gomes, Characterization of the second- and third-harmonic optical susceptibilities of atomically thin tungsten diselenide, Sci. Rep. **8**, 10035 (2018).
[69] M. Lobet, M. Sarrazin, F. Cecchet, N. Reckinger, A. Vlad, J.-F. Colomer, and D. Lis, Probing graphene $\chi^{(2)}$ using a gold photon sieve, Nano Lett. **16**, 48 (2016).
[70] S. Ha, H. Kim, H. Nam, J. Choi, K. Chae, J.-U. Lee, J.-Y. Park, Y. Yoo, and D.-I. Yeom, Enhanced optical third-harmonic generation in phase-engineered $MoTe_2$ thin films, ACS Photonics **9**, 2600 (2022).
[71] A. Autere, H. Jussila, A. Marini, J. R. M. Saavedra, Y. Dai, A. Säynätjoki, L. Karvonen, H. Yang, B. Amirsolaimani, R. A. Norwood, N. Peyghambarian, H. Lipsanen, K. Kieu, F. J. G. de Abajo, and Z. Sun, Optical harmonic generation in monolayer group-VI transition metal dichalcogenides, Phys. Rev. B **98**, 115426 (2018).
[72] J. Pettine, P. Padmanabhan, N. Sirica, R. P. Prasankumar, A. J. Taylor, and H.-T. Chen, Ultrafast terahertz emission from emerging symmetry-broken materials, Light: Sci. Appl. **12**, 133 (2023).
[73] A. Avdoshkin, V. Kozii, and J. E. Moore, Interactions remove the quantization of the chiral photocurrent at Weyl points, Phys. Rev. Lett. **124**, 196603 (2020).
[74] J. Orenstein and J. S. Dodge, Terahertz time-domain spectroscopy of transient metallic and superconducting states, Phys. Rev. B **92**, 134507 (2015).